Dynamics of Remotely Forced Intraseasonal Oscillations off the Western Coast of South America

ALLAN J. CLARKE* AND RIZWAN AHMED†

Oceanography Department, The Florida State University, Tallahassee, Florida

(Manuscript received 23 September 1997, in final form 19 March 1998)

ABSTRACT

Six years of sea level observations at six locations along the South American coast from Peru to Chile were analyzed at intraseasonal frequencies (periodicity 1–2 months). A high-resolution, low-frequency numerical coastal model, having realistic shelf and slope topography and bottom friction and forced by an equatorial signal, was used to analyze the intraseasonal coastal dynamics at these latitudes. The following results were obtained.

1) Lagged correlations between sea level stations imply a sea level poleward propagation of 250 km day^{-1}. The frictionless vertical wall theory poleward phase speed was considerably less at 216 km day^{-1}. Model runs with realistic bottom friction and shelf and slope bottom topography gave poleward phase speeds much closer to that observed. For typical parameters the phase speed was 253 km day^{-1}. Both bottom friction and topography significantly affect the propagation speed.
2) Past work has shown that the sea level amplitude should grow alongshore like $\sqrt{|f|}$ (f = Coriolis parameter). The observed amplitude is much more uniform alongshore, similar to the frictional model with shelf and slope bottom topography.
3) The modeled intraseasonal alongshore velocity field with bottom friction and shelf and slope bottom topography differs considerably from that of the inviscid vertical wall case. Although both have negligible amplitude in the deep sea away from the coast, the velocity amplitude in the more realistic case is trapped along the upper slope with its core at about 1000–1200 m and with decreasing amplitude toward the coast and above the core. Velocity amplitudes in the core are typically about 15 cm s^{-1}.

1. Introduction

Coastal sea levels along the western coasts of North and South America exhibit oscillations of intraseasonal periods (about 30–70 days). These coastal sea level oscillations, first documented by Spillane et al.(1987), propagate poleward along the coast at a speed comparable to that of the first-mode coastal Kelvin wave. Enfield (1987) showed that the coastal signal results from equatorial Kelvin waves that are generated remotely by intraseasonal winds in the western and central Pacific. Along the equator the waves are dominated by vertical-mode 1 and propagate about a quarter of the way around the earth eastward to the eastern Pacific Ocean boundary.

Equatorial wave reflection theory from meridional and nonmeridional eastern boundaries (Moore 1968; Clarke 1983, 1992; Grimshaw and Allen 1988) is qualitatively consistent with these observations. At intraseasonal frequencies, when an incoming vertical-mode 1 Kelvin wave reaches the eastern boundary, some energy may be reflected as westward propagating Rossby waves but most goes to coastally trapped waves propagating poleward into the Northern and Southern Hemisphere.

Coastal Kelvin wave theory predicts how the coastal sea level amplitude should change with distance from the equator and provides an estimate of the likely alongshore flow. Consider first the amplitude behavior. When a coastal Kelvin wave propagates along a coastline like the western coastline of South America, it is trapped to the coast with the radius of deformation trapping scale. Since this scale is proportional to the reciprocal of the Coriolis parameter, the wave energy is confined more and more tightly to the coast as the wave propagates southward, and to conserve energy flux, the amplitude increases like $\sqrt{|f|}$ (Moore 1968). Concerning the alongshore flow, the alongshore current v associated with the intraseasonal coastal Kelvin wave is given at the surface by

$$v = \frac{g\eta}{c}, \tag{1.1}$$

* Additional affiliation: Geophysical Fluid Dynamics Institute, The Florida State University, Tallahassee, Florida

† Current affiliation: Datastream Systems, Inc., Greenville, South Carolina.

Corresponding author address: Dr. Allan J. Clarke, Department of Oceanography, The Florida State University, Tallahassee, FL 32306-4320.
E-mail: clarke@ocean.fsu.edu

where g is the acceleration due to gravity, η the coastal sea level, and c the first vertical-mode phase speed. For a sea level amplitude of only 4 cm and $c = 2.5$ m s^{-1}, the amplitude of the alongshore current is 16 cm s^{-1}. This is quite a strong coastal flow.

But the above theory assumes that the coast is a frictionless vertical wall. In reality it is neither. It is not approximately frictionless because at intraseasonal frequencies ω, the oscillation timescale ω^{-1} is comparable to the frictional spindown times on the shelf and upper continental slope. The coastline cannot be regarded dynamically as a vertical wall because the continental shelf and slope are comparable in width to the baroclinic radius of deformation. These results suggest that bottom friction and shelf and slope topography should fundamentally change the predicted intraseasonal coastal sea level and flow structure. In reality, does the coastal intraseasonal sea-level amplitude increase poleward along the South American coast? Are intraseasonal currents still strong when friction and shelf topography are taken into account? How does the structure of the currents change? Are the changes mainly due to bottom friction, shelf topography, or a combination of both?

These questions have motivated us to analyze and understand the dynamics of remotely forced intraseasonal flows along the western coast of South America when bottom friction and shelf and slope bottom topography are taken into account. The paper is organized as follows. In section 2 we discuss sea level data at six stations along the Pacific South American coastline, and then, in section 3, we describe the phase speed and amplitude of the intraseasonal sea level. Section 4 describes the results of the Clarke and Van Gorder (1994) high-resolution, low-frequency numerical model having realistic stratification, topography, and bottom friction. A comparison of the sea level observations and model results follows in section 5, and section 6 ends the main text with some concluding remarks.

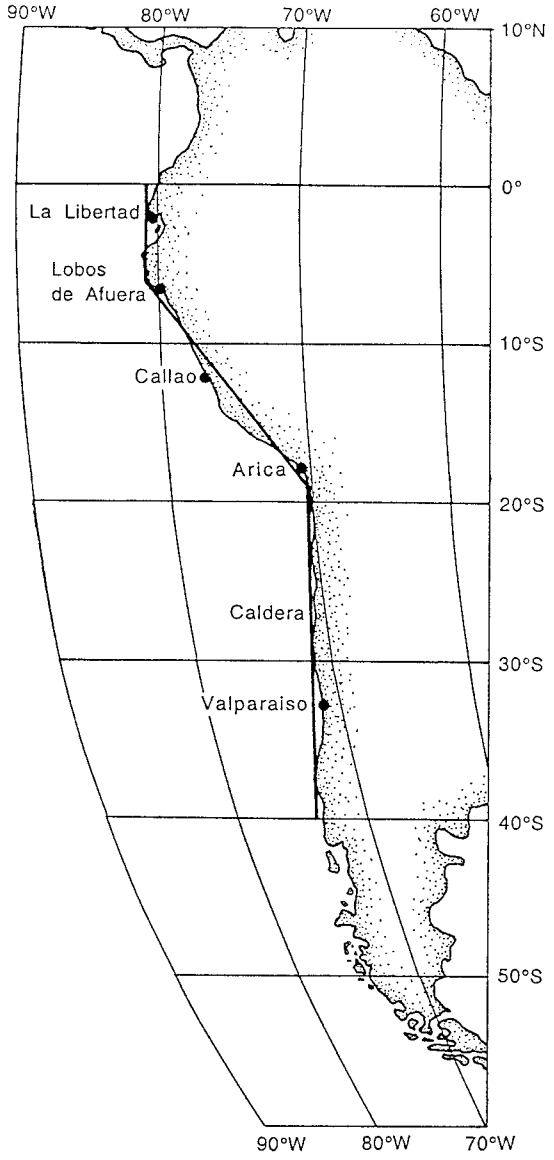

FIG. 1. The six sea level stations along the Pacific South American coastline. The sea level records span a 6-yr period beginning January 1986 and ending 1991. The black solid line from La Libertad to Valparaiso is the boundary used for the coastal numerical computations.

2. The data

Sea level stations used in this study are shown in Fig. 1. Tide gauge records for the years 1986–91 were obtained from the Tropical Ocean and Global Atmosphere (TOGA) Sea Level Center at the University of Hawaii. A 6-yr period, beginning in January 1986 and ending in March 1991, is common to most of the tidal stations along the South American Pacific coast. A smoothed representation of the coastline is used to define an alongshore distance scale with its origin at the equator. By using recent sea level data from 1986 to 1991 we cover a 4500-km stretch of coastline with six sea level stations. There were a few extra stations available, but the time series for these were either too short or far too gappy to reliably estimate a mean daily time series.

The hourly data were first screened for errors and datum shifts. The tides were removed in a similar way to Wong (1987). At each station, the observed hourly tidal signal is represented as S_t ($t = -n, -n + 1, \cdots, 0, \cdots, n - 1, n$) with $t = 0$ being the central time of the record. In our application, the tidal signal was modeled as a sum of 23 frequencies. A least squares fit was then done with the observed sea level in order to obtain the harmonic coefficients, which were then used to get the amplitude of the major components. After subtracting the modeled tidal oscillation from the observed sea level, an hourly gappy sea level time series (from 1986 to 1991) resulted at each station. Most of the gaps in the data were only of a few hours and these were treated as suggested by G. T. Mitchum (1987, personal com-

munication). When gaps occur, they are given zero weight in the filter weighting function and the total weighting is appropriately renormalized. In this way, sometimes gaps in the time series could be filled in. A criterion is available for determining when the interpolated point is likely to be inaccurate so that the point can be flagged as missing. Based on Mitchum's analysis, an interpolated point was flagged as missing if the sum of the absolute value of the filter weights for the gap points was greater than 0.25. Gaps were patched by linear interpolation using data from neighboring stations not otherwise used in the analysis. La Libertad and Valparaiso contained gaps approximately 5% and 3% of their records during the study period, the longest gap being over 5 days. Decimation to daily values gave a 2190-point time series at each station with common start time at 1 January 1986. At each station, the time series were bandpass filtered using a first-order Butterworth function at a periodicity of 30–70 days to obtain the intraseasonal sea level signal. The data were filtered forward and backward in time so that there was no net phase shift. Figure 2 shows the intraseasonal time series at each of the stations.

3. Intraseasonal sea level observations

Below we analyze the phase speed and the alongshore amplitude structure of the intraseasonal sea level records.

a. Phase speed

Lagged correlations were calculated between all sea level record pairs and the maximum correlation coefficients and corresponding lags are shown in Table 1. The correlations of all pairs were significant at the 95% level except the pairs La Libertad–Valparaiso and Lobos–Valparaiso, which were significant at the 90% level. The lag at maximum correlation is plotted as a function of alongshore separation for each record pair in Fig. 3. The regression line corresponds to a poleward sea level propagation speed of 250 $\pm$ 3.5 km day^{-1} (2.89 $\pm$ 0.04 m s^{-1}). Shaffer et al. (1997) found, for adjusted sea level data from 1991 to 1992 on the west coast of South America between 6° and 33°S, a similar poleward propagation speed of 266 km day^{-1} (3.08 m s^{-1}). Romea and Smith (1983) estimated a poleward propagation speed of 260 km day^{-1} (3 m s^{-1}) from data along the western South American coast from 2° and 17°S.

These speeds all differ considerably from the first-mode Kelvin wave phase speed. Although this speed varies in space and time as the stratification varies, it does not vary enough to overlap with the observed phase speeds. For example, Shaffer et al. (1997) calculated the coastal Kelvin wave phase speed at approximately 30°S in February 1992 to be 200 km day^{-1} (2.31 m s^{-1}) while Romea and Smith (1983) calculated 207 km day^{-1} (2.4 m s^{-1}) at 5°S in 1977, 216 km day^{-1} (2.5 m s^{-1}) at 15°S in 1977, and 225 km day^{-1} (2.6 m s^{-1}) at 15°S in 1976. We estimated an average first vertical-mode Kelvin wave phase speed of 221 km day^{-1} using buoyancy frequency N averaged at each depth along the southeastern Pacific boundary from the equator to 40°S (see the profile in Fig. 4). These calculated speeds are all less than those observed. We will address this discrepancy later with a numerical model (see sections 4 and 5).

b. Amplitude structure

To determine the alongshore amplitude structure, we calculated linear regression coefficients between a given station and the others at lags corresponding to maximum correlation. In a least squares sense, this is the best way to estimate the amplitude structure of the intraseasonal sea level signal alongshore. Degrees of freedom for each station pair were calculated as in Davis (1976) and the 90% confidence limits estimated in standard fashion.

The solid line plot in Fig. 5a shows the regression coefficient of the sea level variability at a given station relative to La Libertad. As noted earlier in section 1, if the sea level were described by poleward propagating coastal Kelvin wave dynamics, the sea level amplitude would increase poleward and the regression coefficients relative to La Libertad should therefore all be greater than 1 and increase poleward. In reality (Fig. 5a) the regression coefficients are less than 1 and do not increase poleward. The smallness of the regression coefficients is most likely due to noise in the La Libertad sea level. The noise makes its amplitude larger than that for pure signal, so regression coefficients relative to La Libertad are smaller (see appendix B). Alongshore changes in the regression coefficients relative to La Libertad do, however, indicate alongshore changes in the signal amplitude (see appendix B). The dashed line plot and associated confidence interval in Fig. 5a shows what these alongshore changes would be if the sea level were governed by frictionless vertical coastal wall dynamics [see Eq. (2.15) of Clarke 1992] and the regression coefficients were correct at Lobos de Afuera. Figures 5b and 5c are similar to Fig. 5a but the regression coefficients are relative to Lobos de Afuera and Callao.

In all three figures 5a–c, we see that there tends to be a decrease in measured sea level with distance along the coast, although the decreased amplitude is significant in only a few cases. Decreased amplitude with distance along the coast is opposite to the theoretically predicted increasing amplitude. We also see that in several cases the theoretical and measured sea levels differ significantly with 90% confidence. Regression plots like these were also made relative to each of the last three stations. In these cases, the error bars for each overlapped and therefore theory and observed amplitudes could not be distinguished. Overall, however, it is clear that with high probability the observed sea levels do

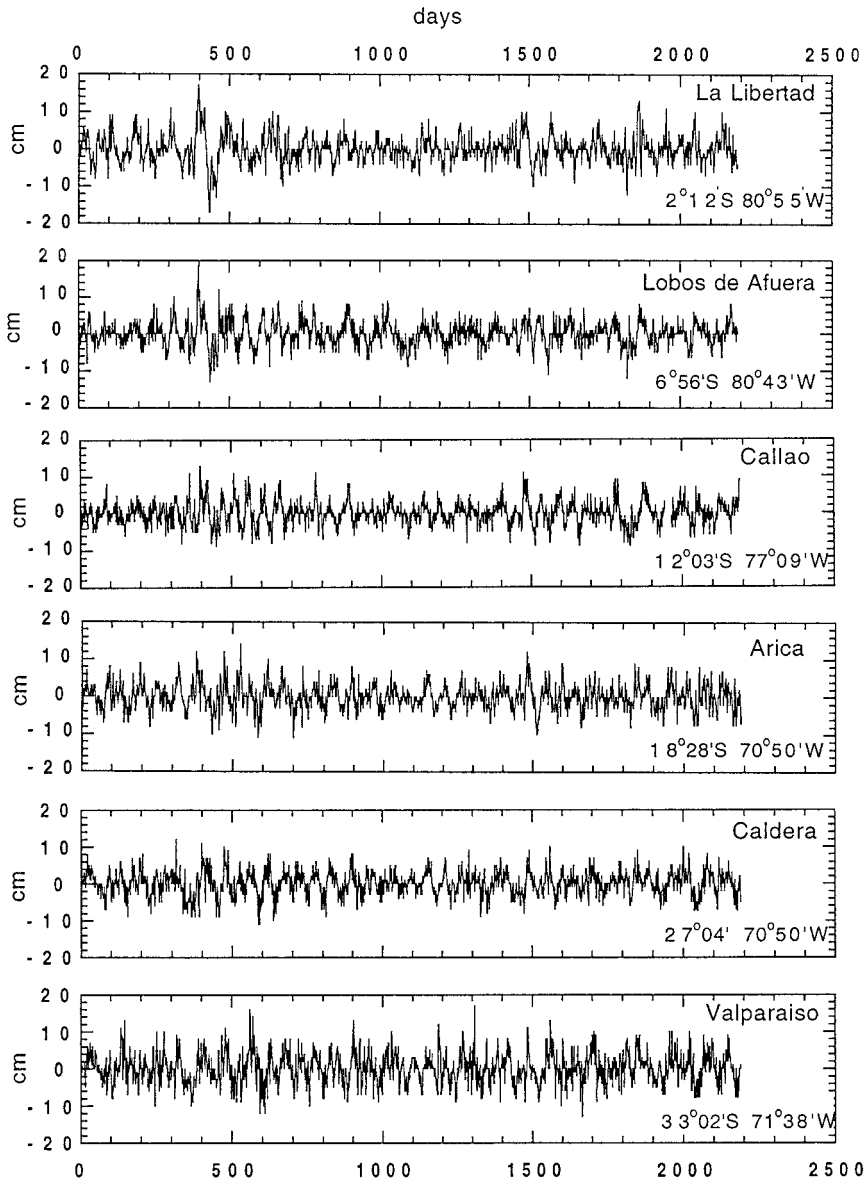

FIG. 2. Intraseasonal sea level time series at the six sea level stations shown in Fig. 1.

TABLE 1. Lag at maximum correlation between all sea level record pairs (lower triangular part of the table) and the corresponding correlation coefficients (upper triangular part of the table). Correlations of all pairs are significant at the 95% level except the pairs La Libertad–Valparaiso and Lobos–Valparaiso, which are significant at the 90% level. The number of degrees of freedom for the significance levels were calculated as in Davis (1976).

	La Libertad	Lobos	Callao	Arica	Caldera	Valparaiso
La Libertad	1	0.6	0.6	0.45	0.45	0.29
Lobos	−3 days	1	0.78	0.61	0.57	0.31
Callao	−5 days	−2 days	1	0.60	0.58	0.31
Arica	−9 days	−6 days	−4 days	1	0.72	0.60
Caldera	−13 days	−10 days	−8 days	−5 days	1	0.72
Valparaiso	−15 days	−13 days	−10 days	−7 days	−3 days	1

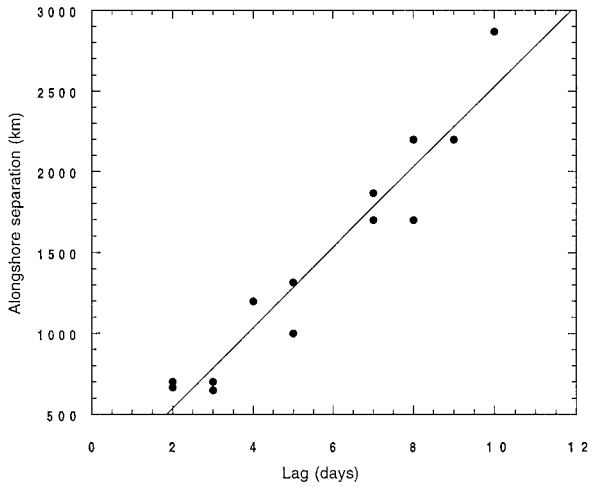

FIG. 3. Lag at maximum correlation versus alongshore separation for all pairs of the sea level series in Fig. 2. Correlations of all pairs were significant at the 95% level except La Libertad–Valparaiso and Lobos–Valparaiso, which were significant at the 90% level. Also shown is the least mean squares linear fit to these points. The line slope gives a poleward propagation speed of 250 km day^{-1}.

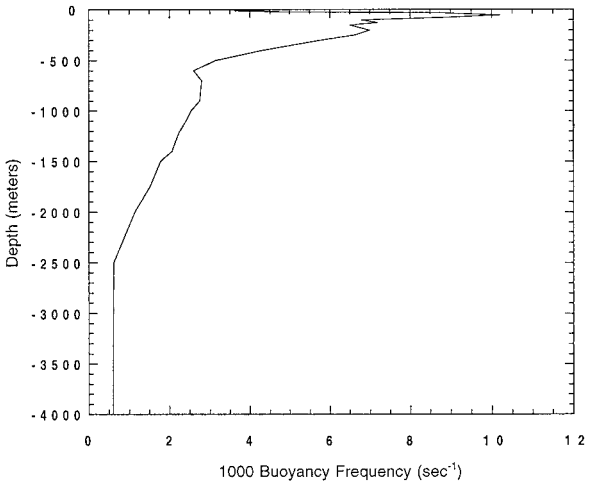

FIG. 4. Buoyancy frequency profile averaged from 74° to 81°W and from 0° to 40°S through the Pacific Ocean. The profile was constructed from data provided by the National Oceanographic Data Center.

not grow as fast as $\sqrt{|f|}$ and may not even increase with distance along the coast.

4. The frictional, shelf and slope topography model

Our intraseasonal model is based on the Clarke and Van Gorder (1994) high-resolution, low-frequency numerical model of the coastal region. The model is linear, essentially continuously stratified, has realistic shelf and slope topography and bottom friction, and is harmonic in time with frequency ω. Since our interest is in the flow near the boundary, rather than solving the problem for the entire Pacific Ocean, we limit our attention to a boundary layer strip extending southward from the equator. The model connects to the equatorial wave guide via an equatorial boundary condition to be discussed later. The Coriolis parameter f varies with latitude and the model coastline approximately follows the shape of the realistic coast in linear segments (see Fig. 1). The field equation and boundary conditions for the slowly varying coastline model are given in appendix A.

Isobaths are everywhere parallel to the coast, so the water depth h is a function only of n, the distance seaward from the coast. The bottom friction τ_B is linearized and evaluated along the sloping bottom $z = -h(n)$ as

$$\tau_B = \rho_o\, r\, \mathbf{u}_B = r(f^{-1}\mathbf{k} \times \nabla p), \qquad (4.1)$$

where $\mathbf{u}_B$ is the geostrophic velocity just above the bottom boundary layer, $r(n)$ is the commonly used bottom friction coefficient, ρ_o the mean water density, $\mathbf{k}$ the unit vertical vector in the upward (z) direction, ∇ the horizontal gradient operator, and p the pressure. The bottom boundary condition follows the analysis of Clarke and Brink (1985) for a thin bottom boundary layer. The analysis shows that the vertical velocity at the bottom is the sum of two parts; one results from the condition of no flow normal to the sloping bottom and the other from Ekman pumping out of the thin boundary layer. The coastal boundary condition (Mitchum and Clarke 1986) states that the depth-integrated flow perpendicular to the model coast is zero at location $n = b$ where the surface and bottom turbulent mixed layers begin to separate. In all cases we assumed $n = b$ corresponds to the 25-m isobath. At the free surface $z = 0$ we used the standard coastal result that the vertical velocity w vanishes. Since the Coriolis parameter f varies with latitude, Rossby waves are possible. The seaward open boundary condition at $n = L$ lets the Rossby waves out without reflection. When Rossby waves are not possible, the boundary condition allows for appropriate decay of the deep sea vertical modes. The nonmeridional boundary condition used here is a slight modification of the meridional one used by Clarke and Van Gorder (1994) (see appendix A).

In order to adequately resolve the shelf and slope topography as well as the vertical variation of the stratification, many grid points are needed. For the (n, z) problem at each s = const section (where n and s are the offshore and longshore coordinates, respectively) we used 151 points in the n direction over a total distance of 200 km and 25 points in the vertical over water depth varying from 25 m at the coast to 4000 m in the constant depth deep sea. To maximize the physical resolution in the vertical, the spacing between the 25 vertical points was stretched in a (WKB) sense by changing the vertical coordinate to

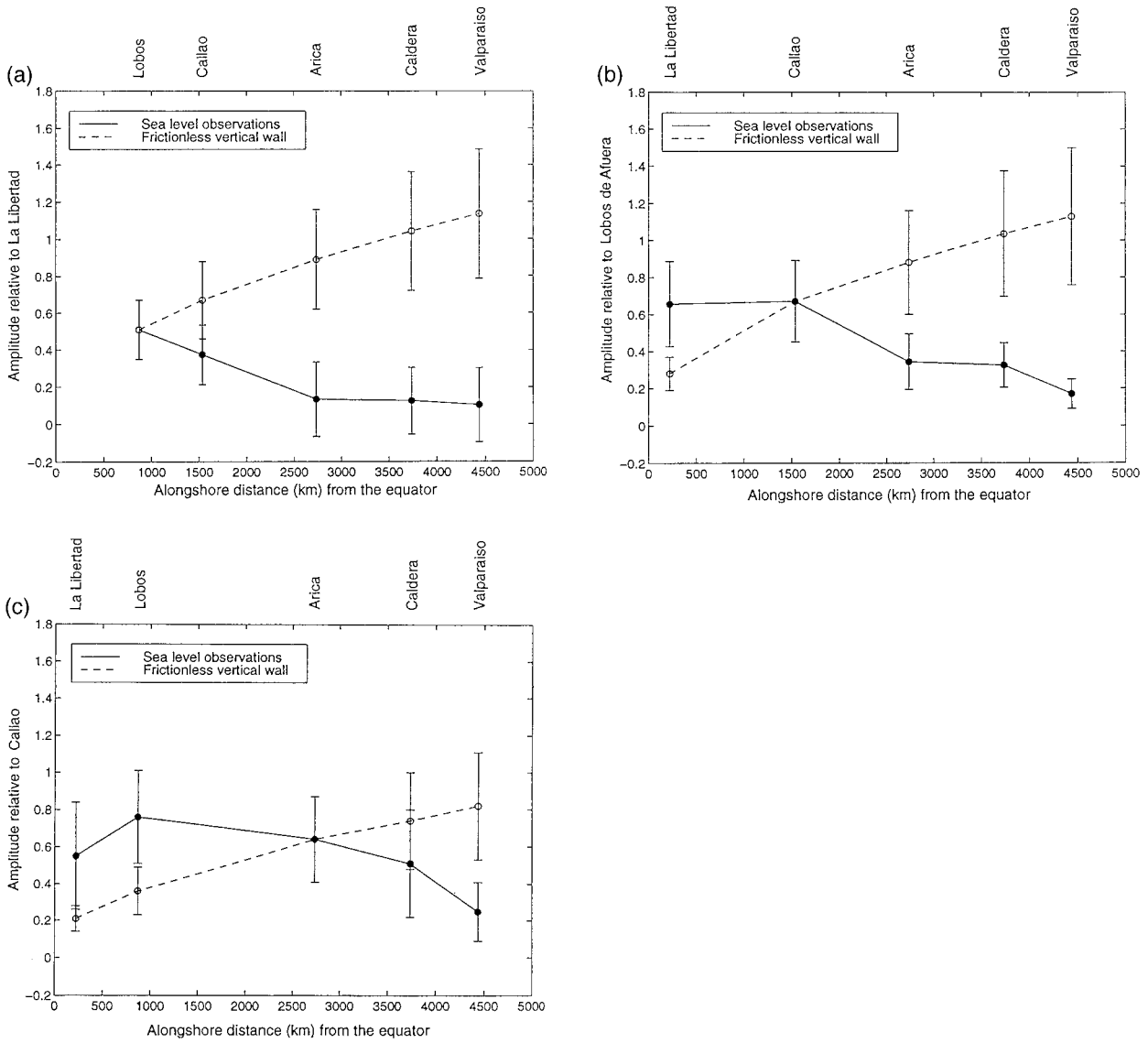

FIG. 5 (a) Comparison (see text) of the regression coefficient plot of the sea level stations relative to La Libertad (solid line) and the corresponding (dashed line) frictionless vertical wall theoretical results computed according to Clarke (1992). Error bars on the observational amplitudes correspond to confidence limits of 90%. The frictionless vertical wall theory indicates how sea level varies alongshore, but information is needed at one location to set the actual size of the regression coefficients at all locations. We matched the theoretical regression coefficient to the observed at Lobos de Afuera, the station adjacent to La Libertad. (b) As for (a), but relative to Lobos de Afuera and using adjacent station Callao to anchor the theoretical plot. (c) As for (a) but relative to Callao and using adjacent station Arica to anchor the theoretical plot.

$$\theta = -\int_0^z N dz \Big/ \int_{-h}^0 N dz, \tag{4.2}$$

where N is the buoyancy frequency. The above choice puts more points where N varies strongly and transforms the problem into a rectangular grid with $\theta = 0$ at the surface and $\theta = -1$ at the variable bottom. The choice is based on the WKB result (Gill 1982)

$$R_j(z) = (N/\overline{N})^{1/2} \cos(j\pi\theta), \tag{4.3}$$

where $R_j(z)$ is the jth vertical eigenfunction and $\overline{N}$ is the vertical average of N from the deep sea bottom to the surface. The finite difference version of the (n, θ) problem was solved at each $s =$ const section by solving the banded matrix corresponding to the finite difference formulation. The $s =$ const sections were 1° apart.

We chose $N(z)$ to be an average profile (Fig. 4) along the southeastern Pacific boundary. Similarly the topography $z = -h(n)$ was taken to be typical of the shelf and slope topography along this boundary. The friction

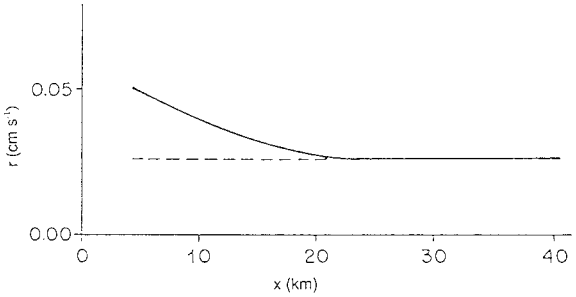

FIG. 6. The friction coefficient $r(n)$.

coefficient $r(n)$ was varied but in the standard case it took reasonable values as shown in Fig. 6. The increase in $r(n)$ over the shelf is primarily due to the influence of surface gravity waves on bottom stress (Grant and Madsen 1979). For most calculations we used a representative intraseasonal frequency of $2\pi/50$ days and, like f, β was allowed to vary alongshore appropriately according to latitude.

The solution is obtained by integrating southward along the coast using backward differences for the alongshore derivative $\partial/\partial s$ (McCreary and Chao 1985). Thus at every alongshore s = const cross section an elliptic problem in n and z, ''forced'' by coastal and bottom pressure available from the previous grid point, is solved. Such an integration assumes that the pressure is known at some initial s = const cross section. The model's starting point for the integration is not at the equator but rather at about 5°S where $(\omega/f)^2 \ll 1$ and the analytical solutions of Clarke (1992) are applicable. Note that the Clarke (1992) results are for a frictionless vertical wall but we expect that the neglect of friction and topography over the first 5° of latitude will negligibly affect the solution. We checked this by starting the integration at 2°, 3½°, and 5° and found that the results were changed negligibly. To summarize in physical terms, the coastal flow is driven by an alongshore pressure gradient associated with a signal that originates at the equator.

To complete the specifications for the model we must choose the mode or combination of modes making up the Clarke (1992) starting solution at 5°S. The analysis of Enfield (1987) for the sea level propagation speed suggests that the intraseasonal signal is dominated by the first vertical mode. Kessler and McPhaden (1995) reported, for the 1991–93 El Niño, intraseasonal Kelvin waves as a prominent part of the equatorial thermocline depth variability. They found that both first and second vertical modes were necessary to represent properly the observed equatorial sea level amplitude. However in our case, initializing with vertical mode 2 shows (Fig. 7) that the coastal intraseasonal signal quickly dies out with increasing distance from the equator. The second vertical mode is probably more sensitive to friction than the first because it has smaller seaward and vertical scales and hence the bottom frictional terms rp_{nn} and rp_{xz} are larger [see (A.10)]. Since the intraseasonal signal due to the second vertical mode damps more quickly, for most of our calculations we started the integration utilizing the Clarke (1992) solution at 5°S and just the first vertical mode. The amplitude of this mode was such that the coastal sea level had an amplitude of 5 cm at 5°S.

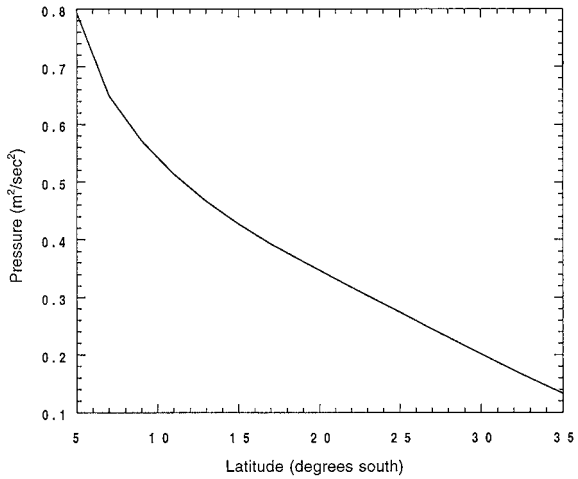

FIG. 7. Pressure amplitude as a function of latitude for an intraseasonal signal initialized with a vertical mode 2 baroclinic Kelvin wave and frequency $\omega = 2\pi/50$ days.

5. Model results and observations

As background to the model results and observations, consider first the inviscid vertical wall theory (Grimshaw and Allen 1988; Clarke 1992). A key result of the theory is that for a given frequency ω a critical latitude exists such that equatorward of the critical latitude the motion propagates offshore and the alongcoast phase speed is infinite while poleward of the critical latitude the phase speed is finite and the motion is trapped to the coast. If the coastline makes an angle θ with due north, then the critical distance $|y|$ from the equator where the solution changes character is (Grimshaw and Allen 1988; Clarke 1992)

$$|y| = \frac{c\cos\theta}{2\omega}, \tag{5.1}$$

where c is the coastal Kelvin wave phase speed. If θ varies alongshore then more than one critical point is possible. A physical explanation of why the solution should change its character has been given in Clarke and Shi (1991). For vertical mode 1 (c = 2.5 m s^{-1}) and the model South American coast (Fig. 1) the critical latitudes corresponding to $|y|$ in (5.1) are respectively 6.2°S, 5.6°S, and 9.0°S for the central intraseasonal frequency $2\pi/50$ days and the band-edge frequencies $2\pi/36$ and $2\pi/73$ days.

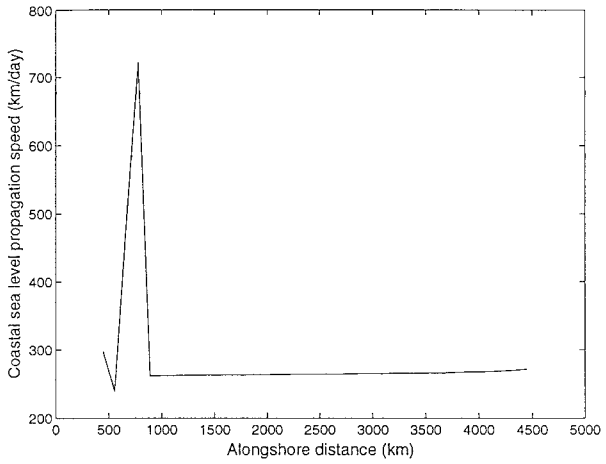

FIG. 8. Model (with bottom friction and topography) coastal phase propagation speed against the alongshore distance s for $\omega = 2\pi/50$ days. The alongshore distance scale has its origin at the equator and is based on a smoothed representation of the coastline (see Fig. 1).

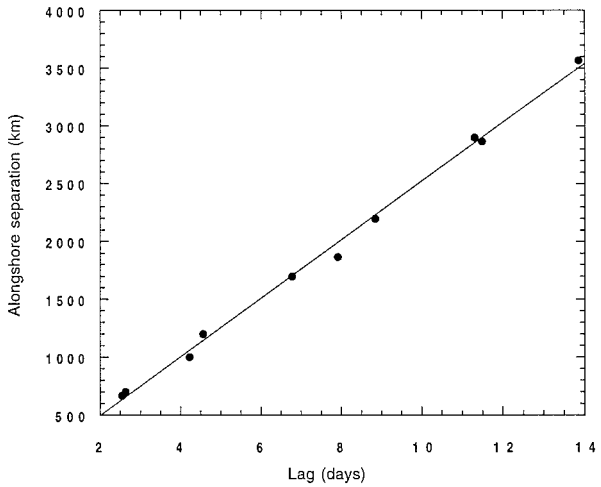

FIG. 9. Theoretical lag between station pairs as a function of alongshore separation for all pairs of sea level series in Fig. 2. The theoretical lag was calculated using a model with friction, shelf and slope bottom topography, and $\omega = 2\pi/50$ days. The linear regression fit gave an average phase speed of 253 km day^{-1}.

a. Coastal sea level phase speeds

Figure 8 shows a plot of model coastal sea level phase speed against the alongshore distance s for the central intraseasonal frequency $2\pi/50$ days. Near the turning latitude (6.2°S) and equatorward of it the phase speed is erratic. Since the inviscid vertical wall solution has coastal phase uniform alongshore equatorward of the critical latitude, we expect phase differences there to be small and accurate phase speed calculations difficult. This and the approximate initialization procedure likely explains the near-equatorial erratic phase speed behavior.

Farther poleward, the phase speed is smoother, increasing slightly from 260 to 268 km day^{-1}. This speed is much faster than the frictionless vertical wall Kelvin wave speed of 221 km day^{-1}. The bigger speed in the more realistic case must be due to some combination of both bottom friction and topography. The slight increase in poleward phase speed is similar to the behavior of the inviscid vertical wall solution of Clarke (1992) for which the phase speed poleward of the critical latitude increases from 216 km day^{-1} to the asymptotic Kelvin wave limit of 221 km day^{-1}.

How do the above model results compare with observations? A plot of lag at maximum correlation between all sea level station pairs against alongshore separation in Fig. 3 gave an average phase speed of 250 $\pm$ 3.5 km day^{-1}. Lags between station pairs against alongshore separation can also be calculated theoretically to obtain a corresponding model estimate. Figure 9 shows the regression fit for the standard case, namely, one for which the model has bottom friction, shelf and slope topography, an intraseasonal frequency of $2\pi/50$ days, and all incident equatorial wave energy in the first vertical mode. The average phase speed in Fig. 9 is 253 $\pm$ 3.8 km day^{-1}, which is very close to that observed. This model value varies slightly with bottom friction, frequency, and the combination of vertical modes that enter the coastal wave guide from the equator (see below), but it is always close to the observed speed.

Table 2 shows the average alongshore phase speed model results for various cases. As one would hope, the best agreement with the observed 250 $\pm$ 3.5 km day^{-1} is for the standard case when bottom friction and shelf and slope bottom topography are included in the model and the central intraseasonal frequency $\omega = 2\pi/50$ days is chosen. At the same frequency the frictionless vertical wall average alongshore phase speed is slower than observed and, when bottom topography is included but not bottom friction, the phase speed is faster than observed. When frequencies $\omega = 2\pi/36$ days and $2\pi/73$ days at the edges of the intraseasonal band are used the phase speed is slightly faster than observed.

The above model phase speed changes can be rationalized as follows. The increase in phase speed when shelf and slope bottom topography is included in the frictionless vertical wall model is consistent with the f-plane coastally trapped wave result (Clarke 1976; Romea and Allen 1984) that the long-wave phase speed is increased by bottom topography with a gentler sloping shelf than continental slope. It is also consistent with the f-plane calculations of Shaffer et al. (1997) for the Chilean coast. The decrease in average phase speed when friction is included is consistent with the scattering of mode-one energy into higher order coastally trapped wave modes, which travel more slowly. The change in phase speed at different frequencies is influenced by two opposing factors. On the one hand, increasing the frequency makes friction dynamically less important and so tends to increase the phase speed. But on the other hand, increasing the frequency pushes the critical lati-

TABLE 2. Average alongshore phase speed model results for different cases. The correlation coefficients are significant at the 95% confidence level. The number of degrees of freedom for the significance levels were calculated as in Davis (1976).

Model	Average phase speed (km day^{-1})	Average phase speed (m s^{-1})	Correlation coefficient
$\omega = 2\pi/50$ days, friction and shelf topography	253 ± 3.8	2.92 ± 0.03	0.95
$\omega = 2\pi/50$ days, frictionless vertical wall	217 ± 2.5	2.51 ± 0.02	0.72
$\omega = 2\pi/50$ days, frictionless and shelf topography	282 ± 4.2	3.26 ± 0.04	0.74
$\omega = 2\pi/36$ days, friction and shelf topography	268 ± 4.0	3.10 ± 0.04	0.82
$\omega = 2\pi/73$ days, friction and shelf topography	273 ± 4.1	3.16 ± 0.04	0.83

tude equatorward, that is, increases the alongcoast distance where the wave travels at a much slower speed and so decreases the average phase speed. Thus in Table 2 we expect that the increase in phase speed when frequency is increased from $\omega = 2\pi/50$ to $2\pi/36$ days is due to friction being dynamically less important while the phase speed increase when the frequency is reduced from $2\pi/50$ days to $2\pi/73$ days is due to the change of critical latitude. The critical latitude effect is stronger for $2\pi/50$ days to $2\pi/73$ days because the change in critical latitude in this case is much larger (from 6.2° to 9.0°S) than for the frequency change $2\pi/50$ days to $2\pi/36$ days (from 6.2° to 5.6°S).

So far, average phase speed calculations have only been presented for the case when the incident equatorial energy is all in vertical-mode 1. The analysis of Kessler and McPhaden (1995) suggests that both the first and second mode were essential to properly represent the equatorial Kelvin wave's observed intraseasonal amplitude. To test the effect of more than one mode we initialized our model with a linear combination of modes in the amplitude ratio mode 1/mode 2 = 4.08/3.38 as in Kessler and McPhaden (1995). The second mode is lagged by 15 days. This is a reasonable approximate lag given the different phase speeds of the vertical-mode 1 and vertical-mode 2 equatorial Kelvin waves and the distance along the equator they have traveled. In this case the average alongcoast phase speed found by regression is slightly lower at 244 km day^{-1}. Runs with frequencies $2\pi/73$ days and $2\pi/36$ days and the same initial vertical mode 1 and vertical mode 2 combination with 15-day lag gave phase speeds 262 and 267 km day^{-1}, respectively. Thus the vertical mode 1 and 2 combination has results very similar to the vertical mode 1 case and the observed phase speed.

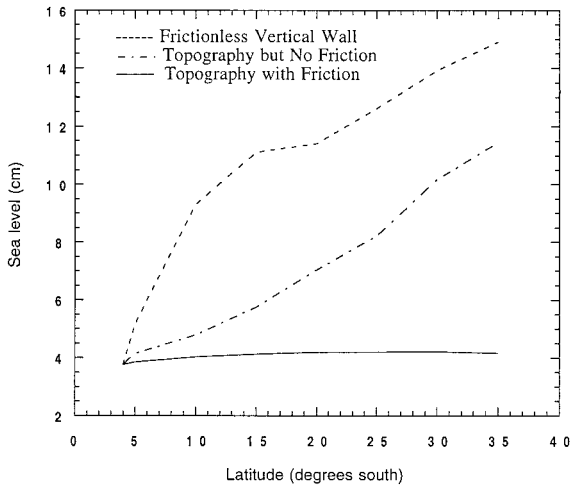

FIG. 10. Comparison of the coastal sea level amplitude of the intraseasonal signal ($\omega = 2\pi/50$ days) for models with topography and bottom friction (solid line), topography but no bottom friction (dash-dot line), and no bottom topography or friction, that is, an inviscid vertical wall (dashed line).

b. Sea level amplitude

Figure 10 shows the coastal sea level amplitude computed for three cases: one with topography and bottom friction, one with topography without bottom friction, and a third with no bottom topography or bottom friction, that is, the theoretical solution for the inviscid vertical wall calculated as in Clarke (1992). The latter solution predicts a $|y|^{1/2}$ growth in sea level amplitude if the coastline were straight; the irregular growth seen in Fig. 10 is due to bends in the coastline. The sea level amplitude for the model with realistic friction and topography is fairly uniform alongshore and differs markedly from the theoretical inviscid vertical wall solution. Figure 10 also shows that, when the model is run with shelf and slope bottom topography but no bottom friction, the bottom topography contributes significantly to the deviation from the coastal Kelvin $\sqrt{|f|}$ amplitude behavior. Thus both shelf and slope bottom topography and bottom friction fundamentally affect the coastal dynamics. Bottom friction lessens poleward amplitude growth because it causes the wave to lose energy as it propagates. Bottom topography sets a seaward trapping scale that does not decrease with latitude like $c/|f|$, so the amplitude growth mechanism is not as effective.

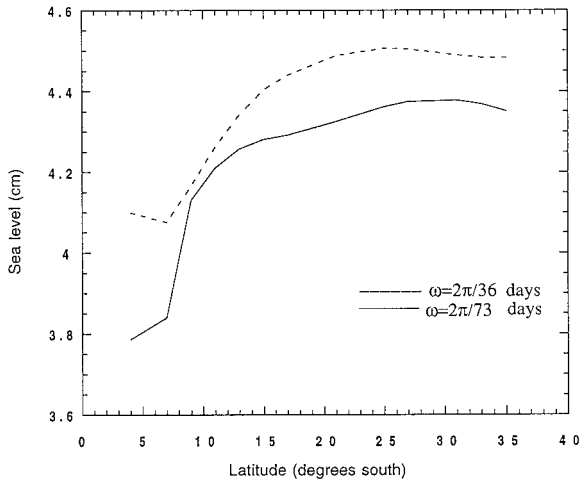

FIG. 11. Pressure amplitude as a function of latitude for the frictional shelf and slope topography model with $\omega = 2\pi/36$ days (dashed line) and $\omega = 2\pi/73$ days (solid line).

The above results were obtained for the central intraseasonal frequency $2\pi/50$ days. As was stated earlier, increased frequency makes friction less dynamically important, so higher frequency should result in a larger (less damped) coastal pressure signal. This is so (see Fig. 11) although the difference is small.

The alongshore nearly uniform coastal sea level amplitude found for the frictional shelf topography model case is consistent with the observed results for coastal sea level amplitude (see Fig. 5 and Fig. 10). This and the model and observed alongshore propagation speed results in section 5a confirm the importance of bottom friction and shelf and slope bottom topography to the dynamics.

c. Coastal currents

Figure 12 shows the amplitude of the alongshore velocity for the frictionless, vertical wall case. We see that away from the equator the velocity amplitude decreases with distance from the coast. It also decreases with depth down to about 1200 m and then increases slightly to the bottom as is appropriate for the first vertical mode. At higher latitudes the velocity field gets trapped closer to the coast with amplitude decreasing away from the coast with radius of deformation scale $c/|f|$, as one would expect for a first vertical mode coastal Kelvin wave. When frictionless bottom topography is included in the model (see Fig. 13), the shelf and slope topography distort the vertical wall profile. While the currents are still coastally trapped and the coastal velocities are large and comparable, the shelf and slope topography case has a subsurface maximum on the upper continental slope at about 250–500 m. The inclusion of bottom friction (Fig. 14) slightly deepens the jet in the deeper water over the continental slope but otherwise does not affect flow seaward of the shelf edge much. However, as one might expect in the shallower water over the continental shelf, the alongshore current is severely decreased by bottom friction. For example, at 31°S the coastal velocity amplitude is 47 cm s^{-1} in the frictionless topography case and only 0.8 cm s^{-1} in the frictional case.

Figure 14b shows the phase of the alongshore velocity for the frictional shelf and slope topography case. The phase in the constant-depth deep sea region is similar to the frictionless vertical wall case (Fig. 12b) in that there is a 180° phase change between 1 and 2 km depth and seaward phase propagation at about the same speed. The 180° phase change at 1200-m depth in the vertical wall case is due to a change in sign of vertical mode 1 at that depth. The seaward phase propagation in the vertical wall case is due to westward phase propagation associated with the β effect. This propagation occurs even though the motion is trapped near the coast (see Figs. 12a and 14a poleward of the critical latitude at 7°S). The more rapid westward phase propagation across the shelf than in the deep sea is due to the influence of bottom topography (topographic β) rather than bottom friction since the phase propagation is seen in the frictionless case (Fig. 13b).

Shaffer et al. (1997) reported results from the first long current meter observations over the continental slope off Chile. These observations near 30°S showed low-frequency fluctuations at periods of about 50 days and with an alongshore current amplitude of 12 cm s^{-1} at 253 m over the continental slope. Although these strong intraseasonal currents are quite similar quantitatively to our model, they differ in structure; the observed currents decrease with depth (see Table 2 of Shaffer et al. 1997) whereas the model currents increase with depth at the same water depth of approximately 900 m (see Fig. 14a). Calculations by Shaffer et al. (1997) for a mode 1 f-plane coastally trapped wave model had current amplitude decreasing with depth but much less than observations. Shaffer et al. (1997) suggested that the mean flow may affect the fluctuating flow. Theory and observations off Oregon indicate that this is possible (Clarke and Lopez 1987). Another reason for the discrepancy between the model results and the observations is that the model does not take into account alongshore variation in bottom topography, which is very strong near the measurement site.

6. Conclusions

Our analysis of six coastal sea levels along the South American coast showed that coastal sea level does not behave like coastal Kelvin-wave sea level at intraseasonal frequencies. Specifically, the observed sea levels propagate poleward faster than coastal Kelvin waves and do not increase in amplitude as the square root of the Coriolis parameter. The discrepancy arises because for coastal Kelvin waves the ''coast'' is a vertical frictionless wall. When shelf and slope bottom topography

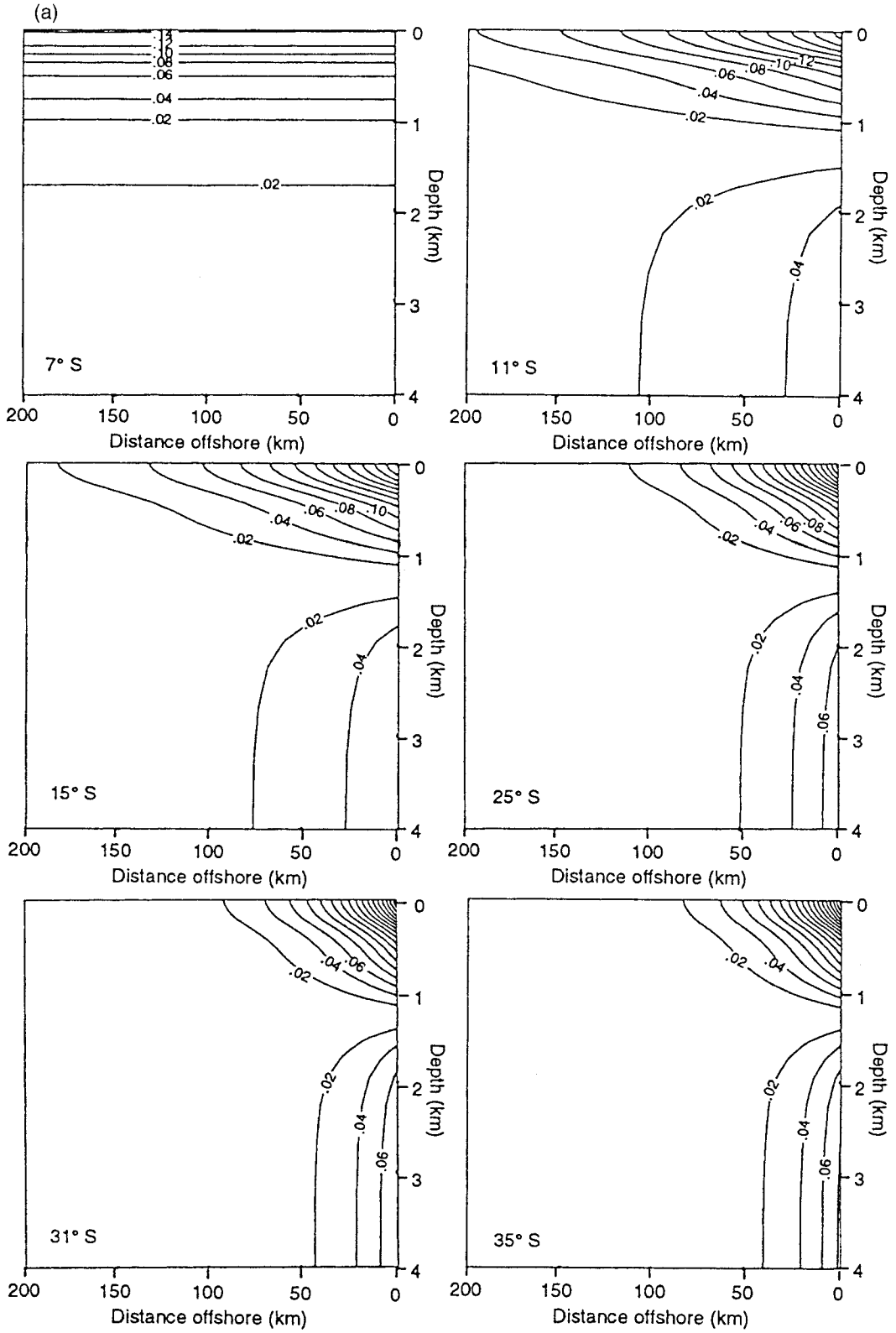

FIG. 12. (a) Amplitude (m s^{-1}) of the alongshore velocity for the frictionless vertical wall case with standard parameters at the six coastal cross sections at 7°S, 11°S, 15°S, 25°S, 31°S, and 35°S. (b) Phase (in degrees) of the alongshore velocity for the frictionless vertical case with standard parameters at the six coastal cross sections at 7°S, 11°S, 15°S, 25°S, 31°S,

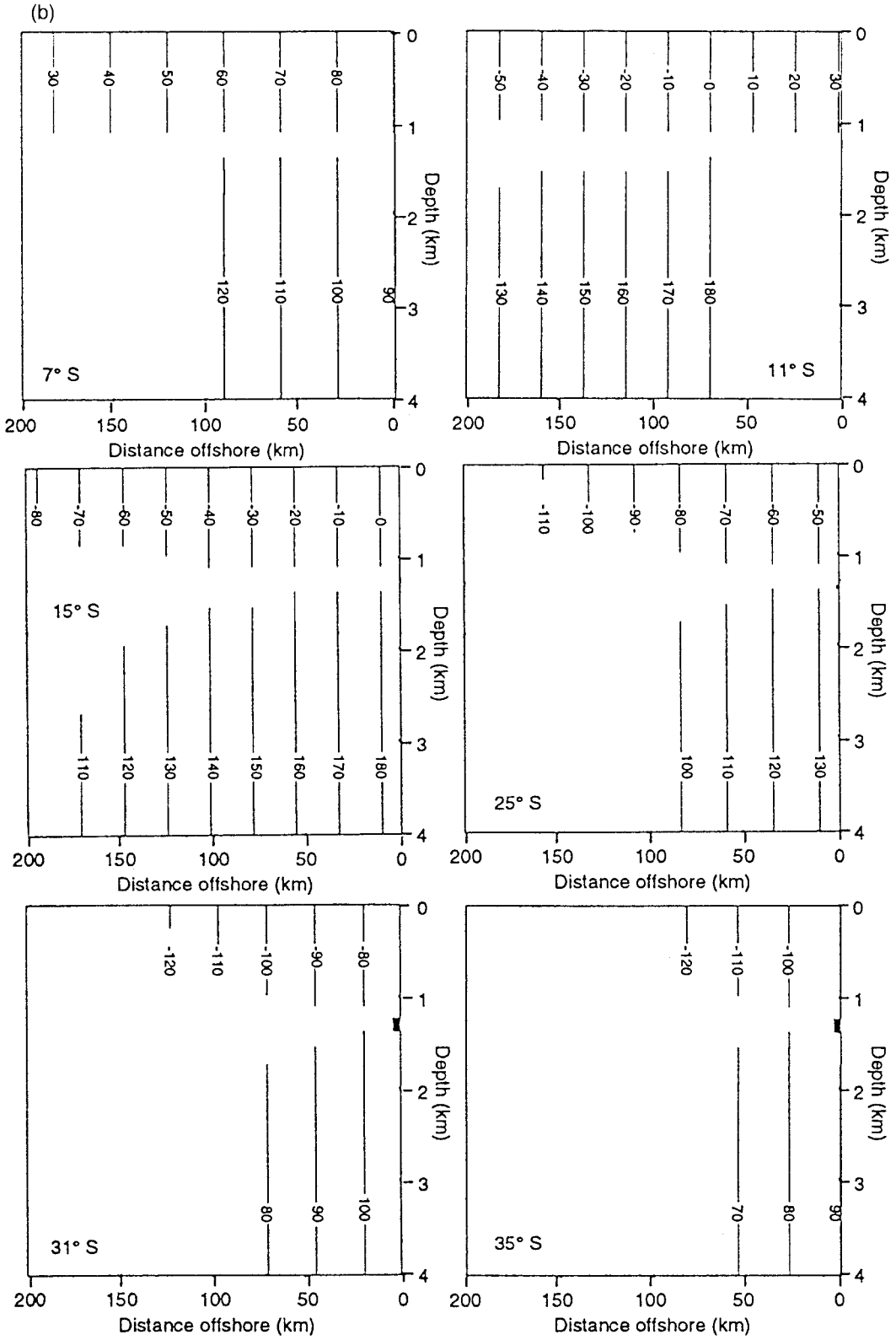

FIG. 12 (*Continued*) and 35°S. Phase is only plotted when the amplitude exceeds 2 cm s^{-1}. The phase is relative to an initial equatorial Kelvin wave phase of zero at the start of the southward integration. Decreasing phase westward corresponds to westward phase propagation.

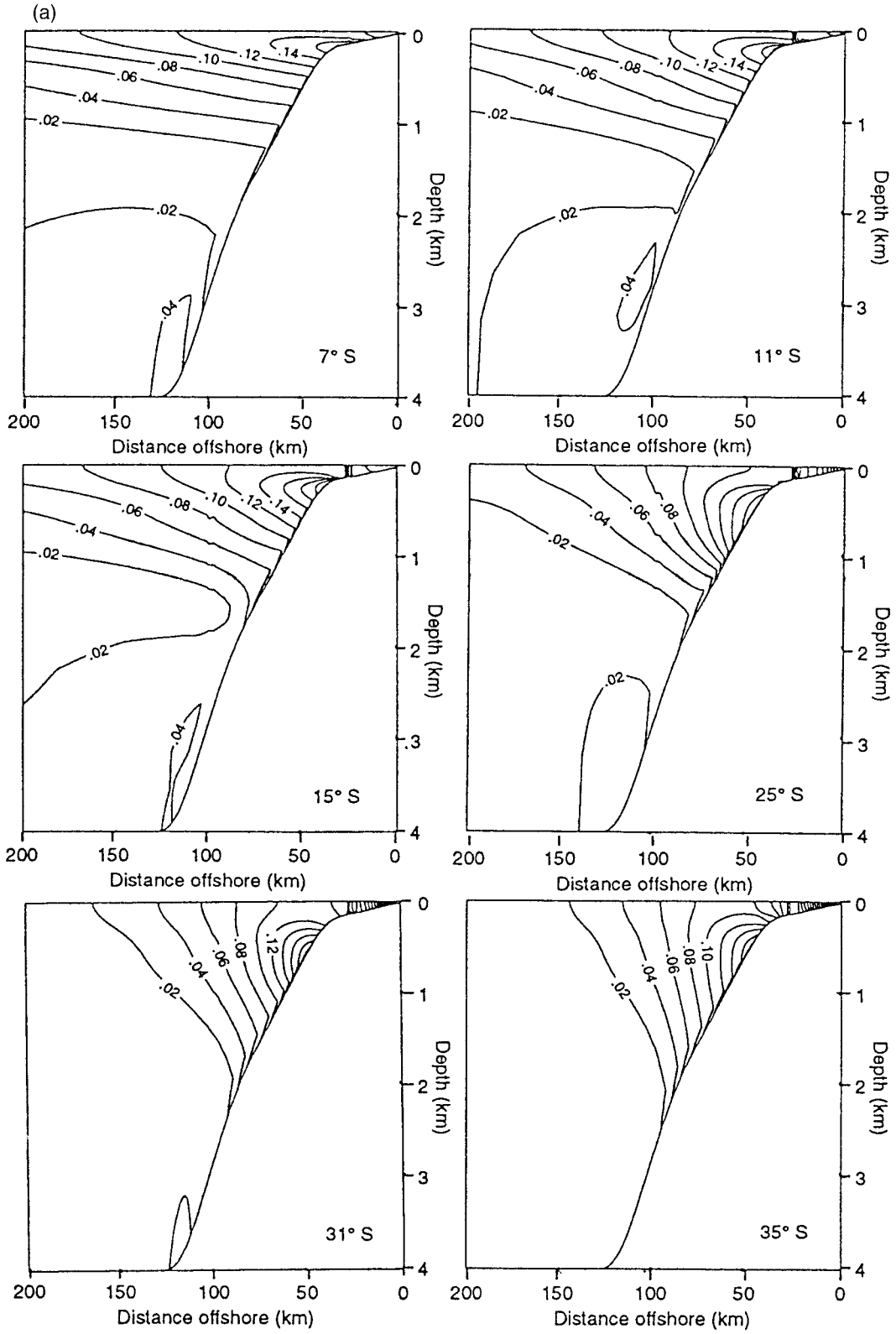

FIG. 13. (a) Amplitude (m s^{-1}) of the alongshore velocity for the frictionless shelf and slope topography case with standard parameters at the six coastal cross sections at 7°S, 11°S, 15°S, 25°S, 31°S, and 35°S. The velocity amplitude over the shelf increases rapidly toward the coast with coastal surface amplitudes 0.14 (7°S), 0.12 (11°S), 0.12 (15°S), 0.31 (25°S), 0.46 (31°S), and 0.56 m s^{-1} (35°S). (b) As for Fig. 12b, but for the phase (in degrees) of alongshore velocity

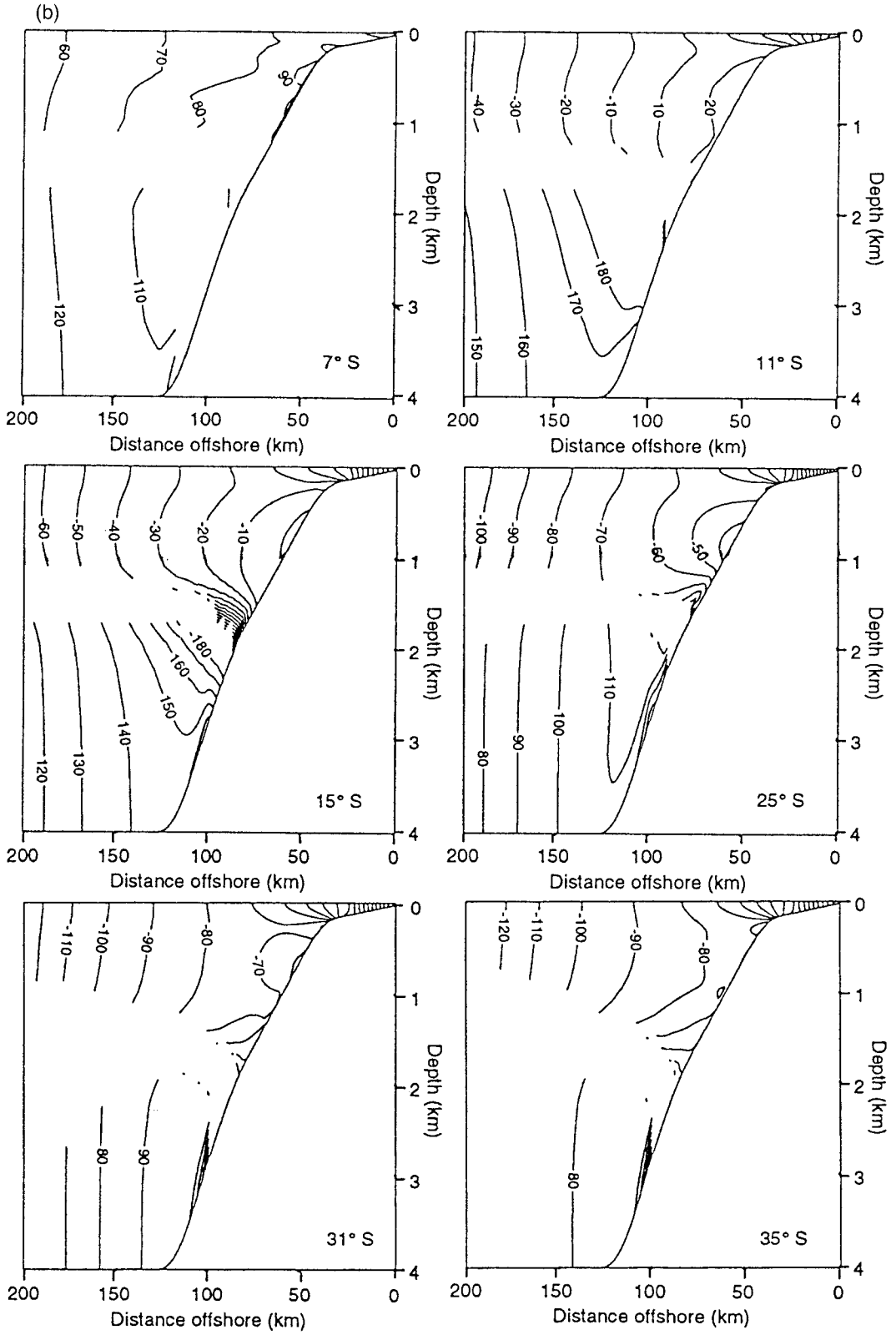

FIG. 13 (*Continued*) for the frictionless shelf and slope topography case with standard parameters. Over the shelf, except for a few grid points the phase decreases monotonically from the coast, that is, as in the deep sea, the phase propagation is westward.

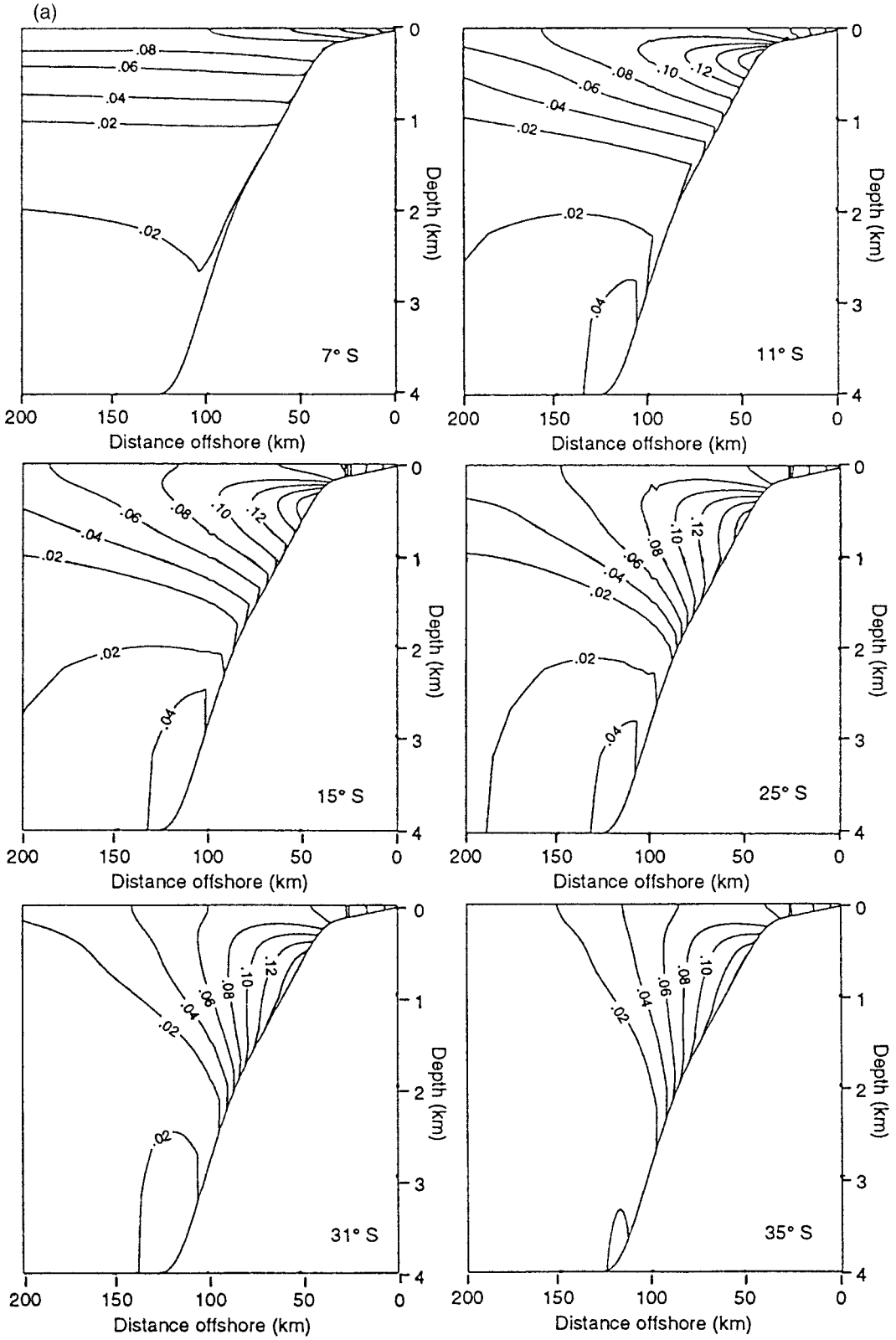

FIG. 14. (a) Amplitude (m s^{-1}) of the alongshore velocity for the frictional shelf and slope topography case with standard parameters at the six coastal cross sections at 7°S, 11°S, 15°S, 25°S, 31°S, and 35°S. Except for a few grid points, the velocity amplitude over the shelf decreases toward the coast. (b) As for Fig. 12b, but for the phase

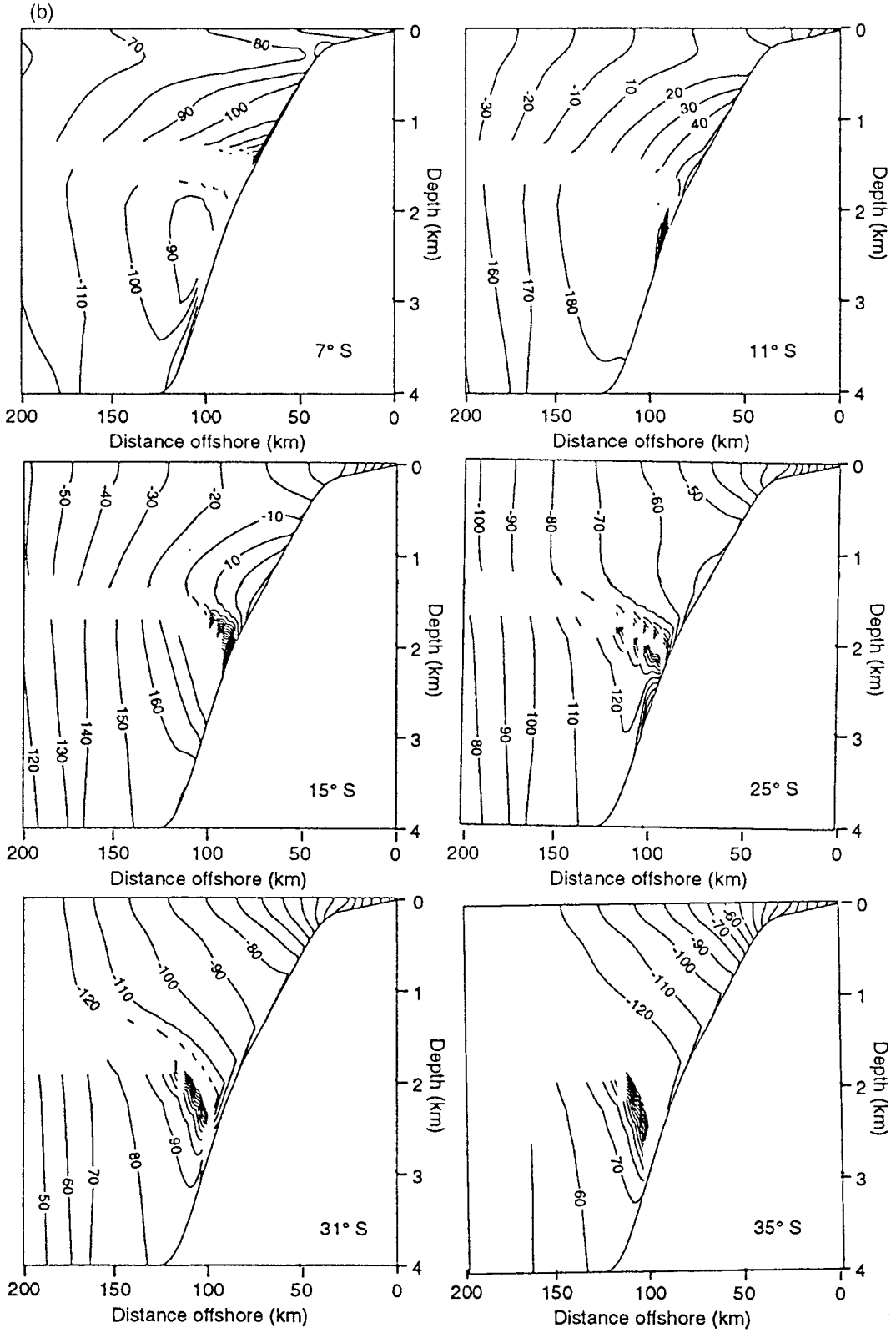

FIG. 14 (*Continued*) (in degrees) of the alongshore velocity for the frictional shelf and slope topography case with standard parameters. Except for a few grid points, on the shelf the phase decreases monotonically from the coast, that is, as in the deep sea, the phase propagation is westward.

and bottom friction are included in a coastal model of the region, the coastal sea level amplitudes and propagation speeds are much closer to those observed. Bottom topography reduces the poleward amplitude $\sqrt{|f|}$ growth because its seaward scale is greater than the radius of deformation trapping scale at nonequatorial latitudes, so the seaward scale for trapped energy does not decrease as fast as $c/|f|$. Bottom friction also reduces the poleward amplitude growth as it causes the wave to lose energy as it propagates poleward. With regard to propagation speed, bottom topography increases it as the wave is no longer a gravity wave but is also influenced by topographic Rossby wave dynamics. Bottom friction reduces it as it scatters the wave energy into higher order modes, which propagate more slowly.

Bottom topography and bottom friction also fundamentally distort the structure of the alongshore flow, but current amplitudes are still quite strong ($\approx$0.15 m s^{-1}). Flows are strongest on the upper continental slope near the bottom at about 250–500-m depth. The model current structure differs from that observed in a region of strong alongshore changes in bottom topography. The discrepancy might be caused by the strong alongshore changes or by a mean alongshore flow since both of these effects are not included in the model.

Acknowledgments. We thank the National Science Foundation (OCE-9415644 and OCE-9617304) for its financial support and the TOGA Sea Level Center at the University of Hawaii for the sea level data.

APPENDIX A

Theory for the Slowly Varying Coastline Case

Normal and tangential coordinates (n, s) are used to define a coordinate system for the problem (see Fig. A1). The origin is at the intersection of the eastern boundary and the equator. The coordinate s is the distance along the boundary from the origin and n is the distance normal to the local coastline. The angle between the unit vector $\mathbf{e}_n$ in the direction of increasing n and the eastward direction is $\theta(s)$.

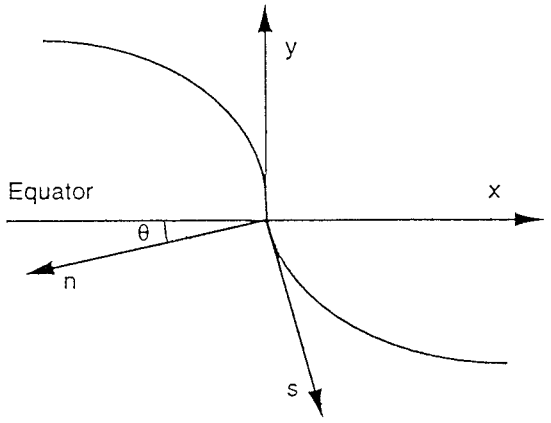

FIG. A1. Normal and tangential coordinates (n, s) and eastward and northward coordinates (x, y). The origin is chosen to be the intersection of the equator and the coastline ($n = 0$). The coordinate n denotes distance landward from the coast and s distance along the coastline from the origin. The angle $\theta(s)$ is marked for $s = 0$.

From Clarke and Van Gorder (1994) we have

$$\left(\frac{\partial^2}{\partial t^2} + f^2\right)\mathbf{u} = -\frac{\boldsymbol{\nabla} p_t}{\rho_o} + f\mathbf{k} \times \boldsymbol{\nabla} p/\rho_o \quad \text{(A.1)}$$

$$w = \left(\frac{-p_{zt}}{\rho_o N^2}\right)_z \quad \text{(A.2)}$$

and

$$\boldsymbol{\nabla} \cdot \mathbf{u} + w_z = 0. \quad \text{(A.3)}$$

In (A.1)–(A.3), z represents distance vertically upward from the ocean surface $z = 0$, t the time, $\mathbf{u}$ the horizontal velocity, w the upward vertical velocity, f the Coriolis parameter, $\mathbf{k}$ the unit upward vector, $\boldsymbol{\nabla}$ the horizontal gradient operator, ρ_0 the constant mean water density, p the perturbation pressure associated with the motion, and N the buoyancy frequency.

For $\omega^2 \ll f^2$ we get, from the substitution of (A.1) and (A.2) into (A.3),

$$\nabla^2 p_t - \frac{2\beta}{f}\mathbf{j} \cdot \boldsymbol{\nabla} p_t + \beta \mathbf{i} \cdot \boldsymbol{\nabla} p + f^2\left(\frac{p_{zt}}{N^2}\right)_z = 0, \quad \text{(A.4)}$$

where $\mathbf{i}$ is the unit eastward vector and $\mathbf{j}$ the unit northward vector. Using the (n, s) coordinate metrics derived in Clarke (1976) (see also Clarke 1977) gives

$$\frac{\kappa p_{nt}}{1 + n\kappa} + p_{nnt} + \frac{1}{1 + n\kappa}\frac{\partial}{\partial s}\left(\frac{1}{1 + n\kappa}\frac{\partial}{\partial s}\right)p_t - \frac{2\beta}{f}\mathbf{j} \cdot \mathbf{e}_n \frac{\partial p_t}{\partial n} - \frac{2\beta}{f}\mathbf{j} \cdot \mathbf{e}_s\left(\frac{1}{1 + n\kappa}\right)\frac{\partial p_t}{\partial s} + \beta \mathbf{i} \cdot \mathbf{e}_n \frac{\partial p}{\partial n} + \beta \mathbf{i} \cdot \mathbf{e}_s \frac{1}{1 + n\kappa}\frac{\partial p}{\partial s} + f^2\left(\frac{p_{zt}}{N^2}\right)_z = 0, \quad \text{(A.5)}$$

where $\kappa(s)$ is the coastline curvature and $\mathbf{e}_n$ and $\mathbf{e}_s$ are unit vectors in the direction of increasing n and s, respectively. Curvature effects can be ignored if the curvature is small enough that over the narrow coastal region of interest $n\kappa \ll 1$ and $\kappa p_{nt}/(1 + n\kappa) \ll \beta \mathbf{i} \cdot \mathbf{e}_n p_n$, that is, $\kappa\omega/(\beta \cos\theta) \ll 1$ where $\theta(s)$ is defined in Fig. A1. Since also $\mathbf{j} \cdot \mathbf{e}_n = \sin\theta$, $\mathbf{i} \cdot \mathbf{e}_s = -\sin\theta$ and $\mathbf{j} \cdot \mathbf{e}_s = \cos\theta$, the field equation (A.5) reduces to

$$p_{nnt} + p_{sst} - \frac{2\beta}{f}\sin\theta p_{nt} - \frac{2\beta}{f}\cos\theta p_{st} + \beta \cos\theta p_n - \beta \sin\theta p_s + f^2\left(\frac{p_{zt}}{N^2}\right)_z = 0. \quad \text{(A.6)}$$

The bottom boundary condition is that (Clarke and Van Gorder 1994)

$$w = -\mathbf{u}\cdot\nabla h + w_{\mathrm{Ek}} = -uh_n + \nabla\cdot(f^{-2}r\nabla p/\rho_o)_{z=-h(n)},$$

where w_{Ek} is the Ekman pumping velocity. In terms of p, this equation can be written

$$\frac{p_{zt}f^2}{N^2} + (p_{nt} + fp_s)h_n + 2f^{-1}\beta r\sin\theta p_n + 2f^{-1}\beta r\cos\theta p_s + r_n p_n + rp_{nn} + rp_{ss} + rp_{nz}(-h_n) + rp_{sz}(-h_n) = 0 \quad \text{on } z = -h(n). \tag{A.7}$$

At intraseasonal frequencies the terms $rp_{nz}(-h_n)$, fh_np_s, and fh_np_{nt} are of the same order so $p_s/p_n \approx r/fd$ or ω/f where d is the vertical scale of the low-frequency flow near the boundary. Since r/fd and ω/f are both $\ll 1$, $p_s \ll p_n$. Thus the field equation (A.6) reduces to

$$p_{nnt} - \frac{2\beta}{f}\sin\theta p_{nt} + \beta\cos\theta p_n + f^2\left(\frac{p_{zt}}{N^2}\right)_z = 0. \tag{A.8}$$

If $(2\omega\tan\theta)/f \ll 1$, then $(2\beta/f)\sin\theta p_{nt}/\beta\cos\theta p_n \ll 1$ and (A.8) reduces to

$$p_{nnt} + \beta\cos\theta p_n + f^2\left(\frac{p_{zt}}{N^2}\right)_z = 0. \tag{A.9}$$

Along the coast of South America from the equator to about 6½°S $\theta \approx 0$ so $(2\omega\tan\theta)/f \ll 1$ near the equator as well as farther south where $|f|$ is bigger. Hence (A.9) holds.

Using $p_s \ll p_n$, the bottom boundary condition can also be simplified. We get

$$\frac{p_{zt}f^2}{N^2} + (p_{nt} + fp_s)h_n + r_n p_n + rp_{nn} - rp_{nz}h_n = 0 \quad \text{on } z = -h(n). \tag{A.10}$$

The other boundary conditions remain the same as the meridional case except that n replaces x and s replaces y. Appendix B of Clarke and Van Gorder (1994) describes the open boundary condition. Everything is the same except that we replace β with $\beta\cos\theta$, $f(y)$ with $f(s)$, and x with n.

In summary, the equations governing the small coastline curvature nonmeridional coastline problem are nearly the same as those for the meridional case. The only differences are that n replaces x, s replaces y, and $\beta\cos\theta$ replaces β.

APPENDIX B

The Effect of Noise on Sea Level Regression Coefficients

Suppose the sea level at one (reference) coastal station is given by

$$\eta(t) = s(t) + \varepsilon(t), \tag{B.1}$$

and at other coastal stations by

$$\eta_j(t) = \alpha_j s(t + \delta_j) + \varepsilon_j(t), \tag{B.2}$$

where $s(t)$ is the coastal sea level signal at the reference station, $\alpha_j s(t)$ is the signal at station j, δ_j is the time the signal at station j lags the signal at the reference station, and ε and ε_j represent uncorrelated noise. The regression coefficient of station j sea level on reference station sea level (adjusted by lag δ_j so that the signal is contemporaneous) is

$$a_j = \frac{\overline{\eta(t)\eta_j(t-\delta_j)}}{\overline{\eta^2(t)}} = \frac{\alpha_j\overline{s^2}}{\overline{s^2} + \overline{\varepsilon^2}}, \tag{B.3}$$

where overbars denote a time average over the record length. Equation (B.3) shows that, even if $\alpha_j > 1$, a_j can be less than one if the noise is large enough. Note, however, that a_j is proportional to α_j and that therefore we can use a_j to determine the way the amplitude of the signal varies alongshore.

REFERENCES

Clarke, A. J., 1976: Coastal upwelling and coastally trapped long waves. Ph.D. thesis, Cambridge University, 178 pp.

——, 1977: Wind-forced linear and nonlinear Kelvin waves along an irregular coastline. *J. Fluid Mech.*, **83,** 337–348.

——, 1983: The reflection of equatorial waves from oceanic boundaries. *J. Phys. Oceanogr.*, **13,** 1193–1207.

——, 1992: Low-frequency reflections from a nonmeridional eastern ocean boundary and the use of coastal sea level to monitor eastern Pacific equatorial Kelvin waves. *J. Phys. Oceanogr.*, **22,** 163–183.

——, and K. H. Brink, 1985: The response of stratified, frictional shelf and slope water to fluctuating large-scale low-frequency wind forcing. *J. Phys. Oceanogr.*, **15,** 439–453.

——, and M. Lopez, 1987: The influence of sloping mean density surfaces on low-frequency shelf water flow. *J. Phys. Oceanogr.*, **17,** 507–517.

——, and C. Shi, 1991: Critical frequencies at ocean boundaries. *J. Geophys. Res.*, **96,** 10 731–10 738.

——, and S. Van Gorder, 1994: On ENSO coastal currents and sea levels. *J. Phys. Oceanogr.*, **24,** 661–680.

Davis, R. E., 1976: Predictability of sea surface temperature and sea level pressure anomalies over the North Pacific Ocean. *J. Phys. Oceanogr.*, **6,** 249–266.

Enfield, D. B., 1987: The intraseasonal oscillation in Eastern Pacific sea levels: How is it forced? *J. Phys. Oceanogr.*, **17,** 1860–1876.

Gill, A. E., 1982: *Atmosphere–Ocean Dynamics.* Academic Press, 662 pp.

Grant, W. D., and O. S. Madsen, 1979: Combined wave and current interaction with a rough bottom. *J. Geophys. Res.*, **84,** 1797–1808.

Grimshaw, R., and J. S. Allen, 1988: Low-frequency baroclinic waves off coastal boundaries. *J. Phys. Oceanogr.*, **18,** 1124–1143.

Kessler, W. S., and M. J. McPhaden, 1995: Oceanic equatorial waves and the 1991–93 El Niño. *J. Climate,* **8,** 1757–1774.

McCreary, J. P., and S. Y. Chao, 1985: Three-dimensional shelf circulation along an eastern ocean boundary. *J. Mar. Res.*, **43,** 13–36.

Mitchum, G. T., and A. J. Clarke, 1986: The frictional nearshore response to forcing by synoptic scale winds. *J. Phys. Oceanogr.*, **16,** 934–946.

Moore, D. W., 1968: Planetary–gravity waves in an equatorial ocean. Ph.D. thesis, Harvard University, 201 pp.

Romea, R. D., and R. L. Smith, 1983: Further evidence for coastal trapped waves along the Peru coast. *J. Phys. Oceanogr.*, **13,** 1341–1356.

——, and J. S. Allen, 1984: The effect of friction and topography on coastal internal Kelvin waves at low latitudes. *Tellus,* **36A,** 384–400.

Shaffer, G., O. Pizarro, L. Djurfeldt, S. Salinas, and J. Rutllant, 1997:

Circulation and low-frequency variability near the Chilean coast: Remotely forced fluctuations during the 1991–92 El Niño. *J. Phys. Oceanogr.*, **27,** 217–235.
Spillane, M. C., D. B. Enfield, and J. S. Allen, 1987: Intraseasonal oscillations in sea level along the west coast of the Americas. *J. Phys. Oceanogr.*, **17,** 313–325.
Wong, K. C., 1987: Tidal and subtidal variability in Delaware's inland bays. *J. Phys. Oceanogr.*, **17,** 413–422.